Comparison of Keypoint Detectors and Descriptors for Relative Radiometric Normalization of Bitemporal Remote Sensing Images

Armin Moghimi, Turgay Celik, *Member, IEEE*, Ali Mohammadzadeh, and Huseyin Kusetogullari, *Member, IEEE*

***Abstract*—This article compares the performances of the most commonly used keypoint detectors and descriptors (SIFT, SURF, KAZE, AKAZE, ORB, and BRISK) in keypoint-based relative radiometric normalization (RRN) of unregistered bitemporal multispectral images. The keypoints matched between subject and reference images represent possible unchanged regions and form a radiometric control set (RCS). The initial RCS is further refined by removing the matched keypoints with a low cross-correlation. The final RCS is used to approximate a linear mapping between the corresponding bands of the subject and reference images. This procedure is validated on five datasets of unregistered multispectral image pairs acquired by inter/intra sensors in terms of RRN accuracy, visual quality, quality, and quantity of the samples in the RCS, and computational time. The experimental results show that keypoint-based RRN is robust against variations in spatial-resolution, illumination, and sensors. The blob detectors (SURF, SIFT, KAZE, and AKAZE) are more accurate on average than the corner detectors (ORB and BRISK) in RRN, with an expense of higher computational cost. The source code and samples of datasets used in this study are made available at https://github.com/ArminMoghimi/keypoint-based-RRN to support reproducible research in remote sensing.**

***Index Terms*—AKAZE, BRISK, change detection, KAZE, keypoint detector and descriptor, keypoint matching, ORB, relative radiometric normalization (RRN), SIFT, SURF.**

I. Introduction

RELATIVE radiometric normalization (RRN) is the process of rectifying radiometric distortions of a multiband subject image with respect to a multiband reference image, acquired by inter/intra sensors on the same scene at different times [1]. RRN is usually applied as a preprocessing operation on multitemporal data prior to their use for remote sensing applications [1]–[3] such as time series image analysis [4], video processing [5], automatic change detection [6], [7], pansharpening [7], and image mosaicking [8].

RRN methods seek to find a linear or nonlinear model based on a radiometric control set (RCS), which is nothing but a set of corresponding pixels between reference and subject images, to rectify radiometric distortions between each corresponding band of the subject and reference images [2]. RRN methods can be broadly classified into two main groups based on how they form the RCS: dense RRN (DRNN) and sparse RRN (SRRN) methods [1]. DRNN methods use the entire set of all pixels in forming the RCS and use global band statistics to learn the parameters of a model for each band of the subject and reference images [1], [2]. Their RRN performances highly deteriorate when the RCS contains a considerable amount of outlier pixels due to changes on the earth surface, or nonlinearities of imaging sensors [1], [9]. In contrast, SRRN methods identify the invariant pixels between the subject and reference images based on their features to form the RCS. Thus, they are more robust against the outliers [2].

Among the SRRN methods, the iteratively reweighted modification of multivariate alteration detection transformation (IRMAD) [10] as an efficient and flexible probabilistic method has been successfully used and further improved for many remote sensing applications, especially for change detection [11]. Bai *et al.* [12] improved on the IRMAD technique to handle complicated radiometric differences caused by temporal changes (e.g., seasonal variations) between the subject-reference image pair by employing kernel canonical correlation analysis and nonlinear regression. Although this method was efficient for RRN of bitemporal multisensor images, including dominant land cover/land use (LCLU) changes, it is prone to overfitting and computationally intensive for dealing with large-size image pairs. Similarly, Denaro and Lin[13] proposed a hybrid IRMAD-based SRRN method to significantly reduce the computational complexity and overfitting by combining the linear and nonlinear CCA and mapping function. Although IRMAD and its improved versions are robust to temporal changes, they only employ band

Manuscript received February 8, 2021; revised March 20, 2021; accepted March 27, 2021. Date of publication March 31, 2021; date of current version April 21, 2021. This work was supported in part by Sichuan Provincial Science, and Technology Projects under Grant 2019JDJQ0023. *(Corresponding author: Turgay Celik.)*

Armin Moghimi and Ali Mohammadzadeh are with the Department of Photogrammetry and Remote Sensing, Geomatics Engineering Faculty, K. N. Toosi University of Technology, Tehran 15433-19967, Iran (e-mail: moghimi.armin@gmail.com; a_mohammadzadeh@kntu.ac.ir).

Turgay Celik is with the School of Electrical and Information Engineering and the Wits Institute of Data Science, University of the Witwatersrand, Johannesburg 2000, South Africa, and also with the School of Information Science and Technology, Southwest Jiaotong University, Chengdu 610031, China (e-mail: celikturgay@gmail.com).

Huseyin Kusetogullari is with the Department of Computer Science, Blekinge Institute of Technology, 37141 Karlskrona, Sweden (e-mail: huseyinkusetogullari@gmail.com).

Digital Object Identifier 10.1109/JSTARS.2021.3069919

TABLE I
DETAILS OF KEYPOINT DETECTORS AND DESCRIPTORS CONSIDERED IN OUR STUDY

Algorithm	Detector type	Descriptor (name/size/type/ information)	Description
SIFT [16]	Blobs	SIFT/128/float/ gradient	It is the most popular keypoint detector/descriptor, which includes four main stages: 1) detecting keypoints from the multi-scale image space, presented by *Difference-of-Gaussians (DoG)* operator (i.e., approximation of *Laplacian-of-Gaussian (LoG)*), 2) keypoint point localization by removing low-contrast and those on edge, 3) assigning orientation(s) to each keypoint based on an orientation histogram, weighted by gradient magnitude and Gaussian-weighted circular window, and 4) providing a unique and robust keypoint descriptor by considering the neighborhood around the keypoint and its orientation histogram.
SURF [17]	Blobs	SURF/64 or 128/float/ gradient	It is based on the determinant of the *Hessian Matrix* which is computed at multi-scale space (i.e., constructed by box filters without computing the whole *Gaussian* scale-space). It also employs integral images to speed up the keypoint detection procedure. The descriptor has been generated by considering the neighborhood around the keypoint and computing the 2D Haar wavelet responses, weighted by a *Gaussian* centered at the feature point.
KAZE [18]	Blobs	M-SURF/64 or 128/float/ gradient	It detects local features based on the scale-normalized determinant of the *Hessian Matrix* through the nonlinear scale space, constructed by nonlinear diffusion filtering. The nonlinear diffusion filtering reduces noise/anomalies and simultaneously preserves important image details (e.g., object boundaries). It employs the Modified–SURF (M-SURF) [19] descriptor, which is more cost-effective and preserves the image structures better than the original SURF descriptor.
AKAZE [20]	Blobs	M-LDB/64/binary/ intensity & gradient	As the name implies, it is a speed-up version of the KAZE detector, which inserts a pyramidal Fast Explicit Diffusion (FED) scheme to speed up feature detection in nonlinear scale space. The highly efficient and low storage descriptor named the Modified-Local Difference Binary (M-LDB) has been identified for this detector to utilize gradient information from the nonlinear scale space.
ORB [21]	Corners	ORB/32/binary/ intensity	It is a combination of modified FAST (Features from Accelerated Segment Test) [22], detection and rotated BRIEF (Binary Robust Independent Elementary Features) [23] descriptor methods. The FAST extractor is first used to detect corner objects as candidate points, and the Harris Corner score is then utilized to refine them from low-quality points. It also employs the improved BRIEF descriptor, which is much more rotation invariant than the original BRIEF descriptor.
BRISK [24]	Corners	BRISK/32 or 64/binary/ intensity	It first extracts corners as feature point candidates using the AGAST algorithm and then refines them with the FAST Corner score in each scale-space pyramid layer. The illumination robust and rotation invariant descriptor has been generated based on each feature's characteristic direction and simple brightness tests.

statistics for RRN, which may not be adequate for accurate normalization of multisensor image pair [14]. To handle this problem, [14] presented a step-by-step approach using the normalized difference water index that automatically exploits the RCS based on the physical characteristics of the land surfaces. Moghimi *et al.* [1] also proposed a robust SRRN method that automatically generates robust, reliable, and spatially distributed RCS using a multistep strategy. Although this method is robust to outliers and anomalies, it is computationally demanding. Recently, Bonnet and Celik [2] proposed an efficient RANdom SAmple Consensus (RANSAC)-based SRRN method, which only uses small pixel subsets to form the linear relationship between image pair, and it is free of calibration of its parameters.

The aforementioned SRRN methods often concentrate on reducing radiometric discrepancies between geo/coregistered image pairs [1], and thus they are limited when RRN of unregistered images is required [9]. These methods cannot adequately handle the radiometric differences between image pairs with different spatial resolutions unless they are resampled to the same spatial resolution [9]. Moreover, the majority of the SRRN methods extract their RCS solely based on the intensity information, which results in low-quality RRN of image pairs with significant illumination and views angle differences. To cope with these limitations, image feature point (or keypoint) detection and matching methods can be efficiently used to form a representative RCS between the reference and subject images. Generally speaking, these methods detect salient keypoints in multiple images, each associated with a keypoint descriptor, and use a similarity metric between the descriptors to find keypoint correspondences (or matches) between the images [15]. These matches are typically invariant to illumination, rotation, and scale variations and thus can be suitable to form a robust and representative RCS [9].

The scale-invariant feature transform (SIFT) [16] and speeded-up robust features (SURF) [17] are among the most commonly used keypoint detectors and descriptors (or keypoint detectors/descriptors in short) [25]. To improve on the performance of SIFT and SURF, several keypoint detectors/descriptors have been introduced, such as KAZE [18], accelerated-KAZE (AKAZE) [20], ORB (oriented FAST and rotated BRIEF) [21], and BRISK (binary robust invariant scalable keypoints) [24]. The characteristics of the keypoint detectors/descriptors considered in this article are summarized in Table I. Fig. 1 demonstrates a wordle to visualize the most common keywords found in keypoint detector/descriptor studies. The wordle shows that SIFT, SURF, KAZE, AKAZE, ORB, and BRISK were among the most commonly used keywords, indicating their popularity in various applications. Moreover, keypoint detectors/descriptors have been frequently used for image matching, and registration [15], [25]. However, to the best of our knowledge, their effectiveness in RRN has rarely been studied. Recently, Moghimi *et al.*[9] proposed a distortion robust method for RRN of unregistered/registered image pair using blockwise KAZE matching and a conditional probability based-regression. Although this study has well demonstrated the importance of image features in RRN, it focuses only on a detector's ability (i.e., KAZE) in the radiometric correction. It does not evaluate the capability of other detectors/descriptors in this way. In order

Fig. 1. Word cloud of the keywords from keypoint detector/descriptor studies.

to fill this gap, we compare SIFT [16], SURF [17], KAZE [18], AKAZE [20], ORB [21], and BRISK [24] for the first time in RRN of unregistered bitemporal image pairs, acquired by inter/intra sensors with same/different spatial resolutions. The performances of keypoint detectors/descriptors are further evaluated in terms of the RRN accuracy, visual quality, quality, and quantity of inliers (correct matches) in the RCS, computing time, and indirect effects on the change detection results.

The remainder of this article is structured as follows. Section II describes the keypoint-based RRN method, details of the five used datasets, and measurement criteria. Section III provides a comparative evaluation of keypoint-based RRN methods in different unregistered image pairs considered in this article. Finally, Section IV concludes this article.

II. Materials and Methods

A. Methodology

Let us consider two unregistered multispectral images R and S, respectively, as reference and subject images with different/similar sizes, acquired by intra/inter sensors over the same geographical region at different times. Let $M_k(P_{R,i}, P_{S,j})$ be a matched keypoint between a keypoint $P_{S,j}(x_{S,j}, y_{S,j})$ of image S and a keypoint $P_{R,i}(x_{R,i}, y_{R,i})$ of image R. The main focus of this study is to test the capability of keypoint detector/discriptor to generate a normalized subject image S^N, in which radiometric differences are minimized. To reach such objective, the main steps of keypoint-based RRN using keypoint are depicted in Fig. 2. In the following, the details of steps involved are discussed.

1) Step (i): Keypoint Detection and Matching: As shown in Fig. 2, the first step aims at identifying a set of matched keypoints between reference (R) and subject (S) images to be used as candidates of the RCS used for the keypoint-based RRN. The contrast of each spectral band of R and S images is first enhanced using *gamma correction* to support the keypoint detection process. The keypoints $P_{R,i}$ and $P_{S,j}$ are then extracted in the form of blobs or corners from each spectral band of image pair using a keypoint detector in Table I. A unique feature vector representation is then assigned to each keypoint $P_{R,i}$ and $P_{S,j}$ based on its neighboring pixels to obtain descriptors $D_{R,i}$ and $D_{S,j}$, respectively. To find matching features in each spectral band, the *nearest neighbor distance ratio (NNDR)* method [16] is adapted as a matching strategy. In this strategy, for each $D_{S,j}$ in S, *L1-norm distance* or *hamming distance* (depending on type of obtained descriptors) is computed to all $D_{R,i}$ in R. The first and second nearest neighbor ${D_{R,i}}^{(1)}$ and ${D_{R,i}}^{(2)}$ are then obtained for each $D_{S,j}$ in S. Finally, the distance ratio $RD = \frac{\mathrm{dist}(D_{S,j}, {D_{R,i}}^{(1)})}{\mathrm{dist}(D_{S,j}, {D_{R,i}}^{(2)})}$ is calculated for each descriptor $D_{S,j}$ to determine whether the potential match point will be accepted or not. The matches with a distance ratio value larger than a threshold are removed form the further analysis. Such a strategy can not completely reduce the risk of false matches and outliers in the matched keypoint set during the feature-matching stage. The majority of matching strategies employ (*RANSAC*) [26] algorithm or its variations to reduce mismatches. However, such algorithms can not accurately handle complex local distortions, especially when the size of images is huge or when the goal is a precise matching of cross-sensor optical satellite images [27]. Hence, *RANSAC* algorithm is first applied to remove extreme outliers, and a triangulated irregular network (TIN)-based local estimation [27] is then employed to remove the rest of the false matches in each spectral band. Finally, all the obtained keypoints identified as inliers (corrected matches) in each spectral band are joined to a set of matched points.

2) Step (ii). Detecting RCS: The second step of the methodology aims at forming a set of reliable RCS using the matched keypoints from the previous step. In this way, digital numbers (DNs) of each M_k is first aggregated from all the spectral bands of R and S images. To enhance the RCS selection accuracy, the possible noise/changed points are further eliminated from the RCS by setting a threshold t on the correlation coefficient between matched pixels of bitemporal images as follows:

$$\rho_k = \frac{\sum_{b=1}^{N_b}\left(Q_{S,k}^b - \overline{Q}_S^b\right)\left(Q_{R,k}^b - \overline{Q}_R^b\right)}{\sqrt{\sum_{b=1}^{N_b}\left(Q_{S,k}^b - \overline{Q}_S^b\right)^2 \sum_{b=1}^{N_b}\left(Q_{R,k}^b - \overline{Q}_R^b\right)^2}} > t \tag{1}$$

where N_b is the number of spectral bands, $Q_{S,k}^b$ and $Q_{R,k}^b$ denote, respectively, DN of the kth match pixel in spectral band b of the R and S images, and $\overline{Q}_S^b$ and $\overline{Q}_R^b$ are their mean values. The range of ρ_k is $[-1, 1]$, and its larger value indicates higher similarity between inliers. Therefore, inlier pixel pairs with a ρ_k larger than the threshold t are selected as RCS pair for further analysis.

3) Step (iii): RRN Model Parameter Estimation: This step aims at generating the normalized subject image S^N by adjusting the image S to the image R through a general form of the linear regression based on the RCS, generated in the previous step as follows:

$$S_b^N = \alpha_b S_b + \beta_b \tag{2}$$

where α_b and β_b are normalization coefficients (gain and offset) for the bth spectral band, estimated through the least-squares method based on the DN values of RCS in R and S images as

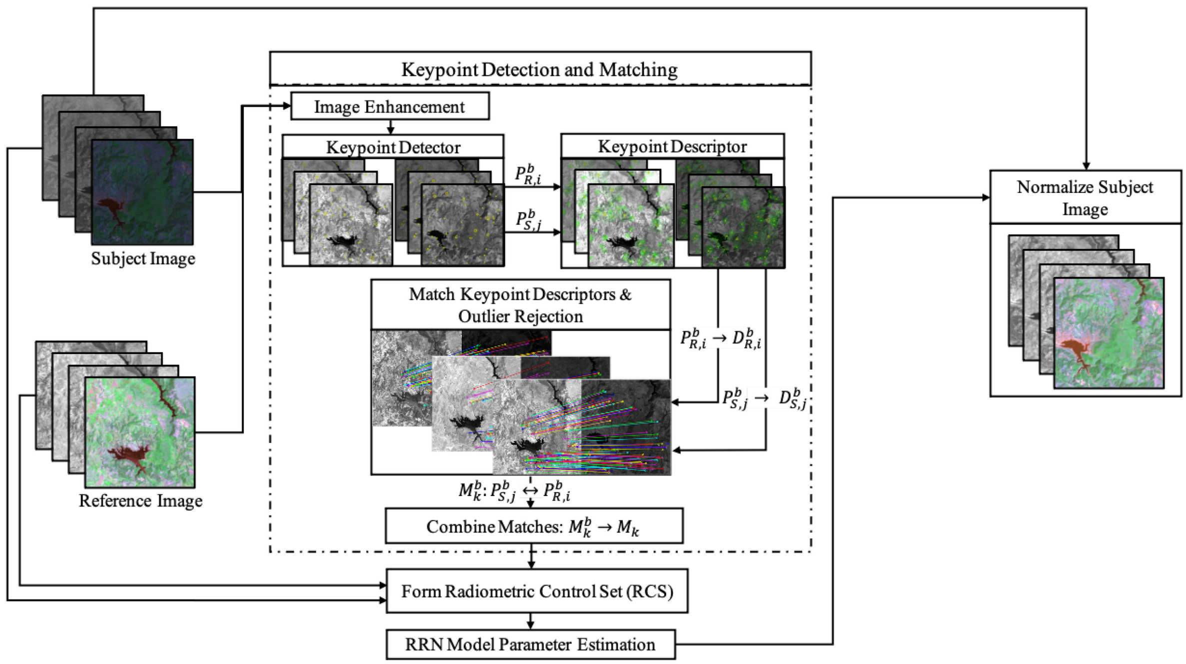

Fig. 2. Keypoint-based RRN.

TABLE II
CHARACTERISTICS OF DATASETS USED IN THIS STUDY

Name	Reference(R)/ Subject(S) Image	Satellite /Sensors/Source	Common Spectral Bands	Resolution (m)	Image size	Date	Study Area
Dataset 1	S	IRS (LISS IV)	Green, Red, NIR	5.5	3000×3000	Jul-2007	Tabriz, Iran
	R				3251×3251	Jul-2008	
Dataset 2	S	Landsat 7 (ETM+)	Blue, Green, Red, NIR, SWIR1, SWIR2	30	582×574	May-2003	Cagliari , Italy
	R				1131×1130	Sep-2002	
Dataset 3	S	IRS (LISS III)	Green, Red,NIR, SWIR	30	2750×2781	Jun-2020	Daggett County, USA
	R	Landsat 5 (TM)		24	2700×2611	Jul-2009	
Dataset 4	S	UK-DMC2	Green, Red, NIR	30	3000×3000	Feb-2012	Cape Town, South Africa
	R	Landsat 5 (TM)		22	2168×2167	Feb-2007	
Dataset 5	S	Google earth	Blue, Green, Red	5	2000×2000	Mar-2020	Bamako, Mali
	R	SPOT 6		1.5	3216×3688	Apr-2018	

follows:

$$\alpha_b = \frac{\sigma^2_{SR,b}}{\sigma^2_{S,b}} \tag{3}$$

$$\beta_b = \mu_R - \alpha_b \mu_S \tag{4}$$

where $\sigma^2_{S,b}$ is the variance of DNs of RCS in the image S, $\sigma^2_{SR,b}$ refers to the covariance between DNs of RCS in R and S images, and μ_S and μ_R denote means of DNs of RCS in R and S images, respectively.

B. Data

We collected five different datasets of unregistered multispectral reference and subject images acquired by different inter/intra sensors under various acquisition conditions as shown in Table II and Fig. 4. It was also assumed that the subject and reference images contain no geo-location information to comprehensively verify the effectiveness of keypoint detectors/descriptors in the keypoint-based RRN method when nongeoreferenced remote sensing images are available. The bitemporal images in Datasets 1 and 2 are acquired by the same sensor (inter-sensor case) in different rows/paths with significant illumination differences. In contrast, the bitemporal images in Datasets 3, 4, and 5 are acquired by different sensors (intrasensor case) with different spatial resolutions and diverse illumination differences. The datasets are used to test the sensitivity of keypoint-based RRN under various imaging conditions.

Dataset 1 from Tabriz, Iran, shows typical characteristics of images captured in urban areas. The keypoint detectors/descriptors are expected to perform well on this dataset because of artificial objects (e.g., buildings) with distinct visual features. Dataset 2 from Cagliari, Italy, is mainly comprised of scenes with different LCs such as rural areas, mountains, vegetation (e.g., farmland and sparse forest), water body and also shows heavy seasonal changes due to the vegetation transition and increase in the surface area of the water body. The keypoint detectors/descriptors are expected to perform moderately well on this dataset because of the presence of textured regions (e.g.,

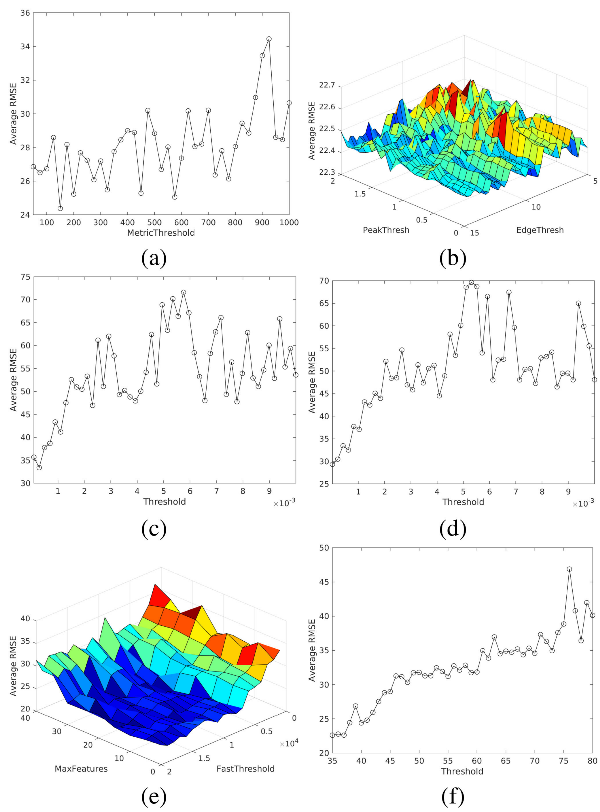

Fig. 3. Grid search to find the optimal parameters of keypoint detectors/descriptors using average RMSE over all datasets: (a) SURF with optimal ‘MetricThreshold’=150; (b) SIFT with optimal ‘EdgeThreshold’=9 and ‘PickThreshold’=1; (c) KAZE with optimal ‘Threshold’=2.92e-4; (d) AKAZE with optimal ‘Threshold’=1e-5; (e) ORB with optimal ‘MaxFeatures’=18 000 and ‘FastThreshold’=20; and (f) BRISK with optimal ‘Threshold’=37.

mountain and sparse vegetation patterns) with diverse image contents. The bitemporal images in Dataset 3 are from Daggett County, USA. The images cover mountainous regions with scattered vegetation patterns and a water reservoir (Flaming Gorge) and show temporal changes, which occurred largely due to cloud covers and their shadows. It is expected that the performance of keypoint detectors/descriptors is adversely affected by the presence of the clouds and their shadows in the subject image. Dataset 4 from Cape Town, South Africa, depicts the characteristics of images acquired on coastal areas. It is expected that the keypoint detectors/descriptors will not be able to completely handle radiometric distortions from this dataset, mainly due to the presence of large texture-free regions (e.g., water bodies and bare soil). Dataset 5 from Bamako, Mali is comprised of a moderately high-resolution image pair covered by a semiurban area with diverse image contents. The keypoint detectors/descriptors are expected to exhibit reasonably good performance on this dataset due to the distinct image features in high-resolution images.

C. Evaluation Criteria

The quality and performance of each keypoint detector/descriptor in RRN procedure is evaluated using the root mean square error ($RMSE$), normalized total gradient (NTG) [28],

TABLE III
OVERVIEW OF KEYPOINT DETECTOR/DESCRIPTOR FUNCTION SETTINGS FOR SURF (MATLAB), SIFT (VLFEAT), KAZE (OPENCV), AKAZE (OPENCV), ORB (OPENCV), AND BRISK (OPENCV)

Method	Function	Descriptor size
SURF	detectSURFFeatures(···,'MetricThreshold',150)	64 Bytes
SIFT	vl_sift(···,'EdgeThresh',9,'PeakThresh',1)	128 Float
KAZE	cv.KAZE('Threshold',2.92e-4)	64 Bytes
AKAZE	cv.AKAZE('Threshold',1e-5)	64 Bytes
ORB	cv.ORB('MaxFeatures',18000,'FastThreshold',20)	32 Bytes
BRISK	cv.BRISK('Threshold',37)	64 Bytes

Note that use of “···” in functions represents the rest of parameters with default settings.

and mean absolute percentage error (MAPE), which are calculated for each spectral band as follows:

$$\mathrm{RMSE} = \sqrt{\frac{1}{N_t}\sum_{j=1}^{N_t}\left(R_j - S_j^N\right)^2} \tag{5}$$

$$\mathrm{NTG} = \frac{\sum_l \left\|\nabla_l\left(S^N - R\right)\right\|_1}{\sum_l\left(\|\nabla_l S^N\|_1 + \|\nabla_l R\|_1\right)} \tag{6}$$

$$\mathrm{MAPE} = \frac{1}{N_l}\sum_{t_l=1}^{N_l}\left|\frac{R_{t_l} - S_{t_l}^N}{R_{t_l}}\right| \tag{7}$$

where R and S^N denote the reference and normalized subject images, respectively, N_t is the total number of pixels of the overlap between R and S^N, N_l represents the number of test samples in specific LCLU, operator ∇_l, with $l \in \{x, y\}$, refers to the image derivative along the direction l, and $\|.\|_1$ is L_1-norm. The lower the value of $RMSE$ and NTG better RRN is

III. EXPERIMENTAL RESULTS AND ANALYSIS

A. Experimental Setup

We implement the keypoint-based RRN in MATLAB (version 2020a) using OpenCV (version 3.4.1) and VLFeat [29] libraries on a desktop computer with Intel(R) Core(TM) i7-3770 CPU@3.40 GHz,12.00 GB RAM, running Windows 8.1.[1]

In experiments, the keypoints between the subject and reference images were matched based on the NNDR with a distance ratio threshold of 0.75. RANSAC with 2000 iterations and TIN-based local strategy with a threshold of 1 pixel was employed to reject the false matches (or outliers). The cross-correlation threshold in RCS selection was set as 0.5 to reject the possible changed/noise pixels. Fig. 3 provides a summary of keypoint detectors/descriptors and the corresponding MATLAB functions with parameters. Each keypoint detector/descriptor has a set of parameters that needs to be set appropriately. Although default settings of the parameters of keypoint detectors/descriptors may yield good performance, we applied grid search on certain parameters of keypoint detectors/descriptors as listed in Table III that can benefit from fine-tuning by considering the average RMSE on all datasets. This process also aims to perform a fair

[1]The source code and samples of datasets used in this study are made available at https://github.com/ArminMoghimi/keypoint-based-RRN to support reproducible research in remote sensing.

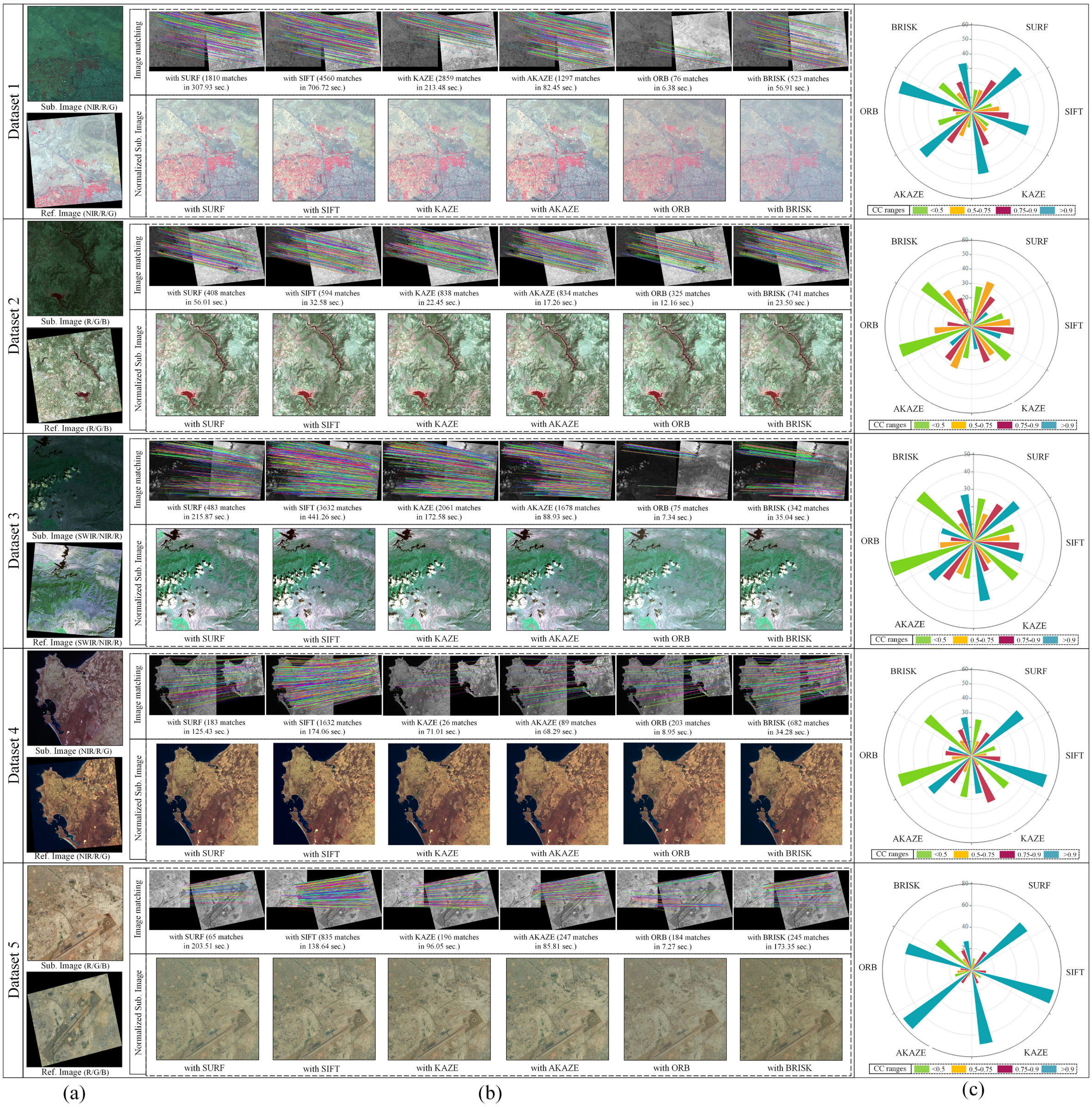

Fig. 4. Keypoint-based RRN results on different datasets: (a) Subject (Sub.) and reference (Ref.) images in each dataset; (b) Normalized subject images (bottom) using different keypoint detectors/descriptors; and (c) The percentage of inliers, generated by the keypoint detectors/descriptors with different cross-correlation ranges.

comparison between different keypoint detectors/descriptors considered in this article. The results from the grid search are shown in Fig. 3 and optimal parameter values are tabulated Table III.

B. Results and Discussion

The qualitative and quantitative results from the experiments are given in Fig. 4 and Table IV, respectively. Table IV shows that the application of keypoint-based RRN on all datasets results in significantly lower RMSE and NTG between the reference and normalized subject images on all bands in comparison to the same metrics computed for the reference and subject (raw) images only. In terms of average RMSE, KAZE achieved the best results on all datasets, but Dataset 2 and 4, where ORB and SIFT, respectively, yielded the best results. For instance, KAZE-based RRN reduced the raw average RMSEs by 81.34%, 67.39%, and 73.12% for the Datasets 1, 3, and 5 while using the ORB and SIFT decreased the raw average RMSEs by 75.99%, and 19.80% for the Dataset 2 and 4, respectively. Considering the average NTG, SIFT-based RRN performs best on all datasets but Dataset 1 and 5, in which KAZE and SURF achieve the best performance, respectively. This result indicates that the normalized subject images generated by the SIFT-based RRN are more robust to local intensity variations than the other ones. Overall, ORB-based RRN yielded the worst results for almost all datasets regarding RMSE and NTG values. SURF- and AKAZE-based RRN achieved moderate results in most cases. The results in Table IV also show that the “blob” detectors (SURF, SIFT, KAZE, and AKAZE) in general perform better than the “corner” detectors (ORB and BRISK).

TABLE IV
PERFORMANCE OF KEYPOINT-BASED RRN WITH DIFFERENT KEYPOINT DETECTORS/DESCRIPTORS IN TERMS OF RMSE, NTG, AND COMPUTING TIME (IN SECONDS)

Data	Method	Blue		Green		Red		NIR		SWIR1		SWIR2		Average		Computing Time (s)
		NTG	RMSE	NTG	RMSE	NTG	RMSE	NTG	RMSE	NTG	RMSE	NTG	RMSE	NTG	RMSE	
Dataset 1	Raw	—	—	0.491	110.60	0.462	91.43	0.539	136.50	—	—	—	—	0.497	112.84	—
	SURF	—	—	0.467	18.90	0.451	24.15	0.499	21.40	—	—	—	—	0.472	21.48	308.96
	SIFT	—	—	0.468	19.03	0.454	24.38	0.503	21.88	—	—	—	—	0.475	21.77	**708.75**
	KAZE	—	—	0.459	18.50	0.450	23.63	0.496	21.02	—	—	—	—	**0.468**	**21.05**	216.28
	AKAZE	—	—	0.486	19.99	0.476	25.12	0.514	23.34	—	—	—	—	0.492	22.82	82.48
	ORB	—	—	0.518	24.63	0.510	28.60	0.511	19.76	—	—	—	—	**0.513**	**24.33**	**6.41**
	BRISK	—	—	0.496	20.23	0.467	24.68	0.479	19.57	—	—	—	—	0.481	21.50	58.76
Dataset 2	Raw	0.532	108.20	0.475	101.51	0.521	100.41	0.540	126.95	0.543	139.05	0.542	129.95	0.525	117.68	—
	SURF	0.347	30.28	0.354	33.15	0.379	35.82	0.440	32.24	0.358	23.16	0.333	19.79	0.369	**29.07**	**58.70**
	SIFT	0.347	29.10	0.354	31.81	0.379	34.19	0.442	32.73	0.358	23.12	0.333	19.44	**0.369**	28.40	33.81
	KAZE	0.357	29.96	0.364	33.00	0.388	34.99	0.445	31.78	0.365	22.76	0.343	19.45	0.377	28.65	23.38
	AKAZE	0.354	29.61	0.361	32.91	0.386	35.33	0.447	32.68	0.363	22.57	0.340	19.44	0.375	28.76	20.33
	ORB	0.366	28.68	0.375	34.83	0.396	36.03	0.454	32.26	0.386	18.72	0.359	19.00	**0.389**	**28.25**	**14.13**
	BRISK	0.353	28.91	0.357	33.65	0.382	35.66	0.443	31.80	0.365	20.80	0.341	19.00	0.374	28.30	25.65
Dataset 3	Raw	—	—	0.528	98.56	0.497	91.76	0.493	92.27	0.470	96.46	—	—	0.497	94.76	—
	SURF	—	—	0.429	27.88	0.416	29.06	0.444	34.19	0.432	36.44	—	—	0.430	31.89	217.54
	SIFT	—	—	0.435	27.69	0.419	28.59	0.437	33.66	0.424	37.46	—	—	**0.429**	31.85	**442.48**
	KAZE	—	—	0.452	27.22	0.452	28.21	0.424	33.12	0.433	35.06	—	—	0.441	**30.90**	174.73
	AKAZE	—	—	0.444	27.66	0.445	28.49	0.425	32.11	0.433	36.36	—	—	0.437	31.15	90.66
	ORB	—	—	0.508	31.18	0.512	33.30	0.481	43.43	0.489	44.14	—	—	**0.497**	**38.01**	**8.31**
	BRISK	—	—	0.464	29.56	0.458	30.37	0.442	37.85	0.445	38.54	—	—	0.452	34.08	36.36
Dataset 4	Raw	—	—	0.475	20.67	0.476	25.10	0.514	35.28	—	—	—	—	0.488	27.01	—
	SURF	—	—	0.400	14.05	0.417	23.87	0.450	27.49	—	—	—	—	0.422	21.80	128.64
	SIFT	—	—	0.392	13.52	0.409	23.87	0.443	27.59	—	—	—	—	**0.415**	**21.66**	**176.43**
	KAZE	—	—	0.500	14.04	0.515	24.73	0.523	28.69	—	—	—	—	**0.513**	22.49	72.83
	AKAZE	—	—	0.426	13.60	0.443	23.74	0.465	28.30	—	—	—	—	0.445	21.88	70.42
	ORB	—	—	0.409	14.54	0.428	24.18	0.455	29.07	—	—	—	—	0.431	**22.59**	**10.27**
	BRISK	—	—	0.438	14.105	0.454	24.554	0.472	28.560	—	—	—	—	0.455	22.41	36.89
Dataset 5	Raw	0.764	74.22	0.762	62.11	0.768	72.40	—	—	—	—	—	—	0.765	69.58	—
	SURF	0.400	14.05	0.417	23.87	0.450	27.49	—	—	—	—	—	—	**0.422**	21.80	**205.57**
	SIFT	0.539	21.07	0.542	18.42	0.555	17.93	—	—	—	—	—	—	0.546	19.14	141.60
	KAZE	0.510	20.19	0.519	17.95	0.534	17.96	—	—	—	—	—	—	0.521	**18.70**	98.57
	AKAZE	0.526	20.89	0.530	18.35	0.546	17.77	—	—	—	—	—	—	0.534	19.00	87.39
	ORB	0.527	20.46	0.535	18.26	0.548	17.85	—	—	—	—	—	—	**0.537**	18.86	**8.44**
	BRISK	0.515	20.895	0.529	21.017	0.553	23.948	—	—	—	—	—	—	0.532	**21.95**	177.96

The best performance is highlighted in blue and the worst in red.

Considering computing times in Table IV, AKAZE, ORB, and BRISK, which employ binary descriptors, result in faster RRN compared to other keypoint detectors/descriptors. ORB-based RRN achieves the minimum computing times for all datasets, which BRISK-based RRN follows. However, BRISK's computing time depends on the number of image features (e.g., edges and corners), as such, for it requires higher computing time for Dataset 5 with the highest spatial-resolution. SIFT- and SURF-based RRN results in the highest and second-highest computing times. This is mainly due to the Gaussian scale-space representation of SIFT and its approximation in SURF.

As shown in Fig. 4(b), the normalized subject images generated by blob detectors for all datasets are considerably similar to the corresponding reference images in terms of perceived brightness and color. The performance of corner detectors was relatively similar to that of blob detectors in generating the normalized images on low/medium spatial-resolution datasets (e.g., Dataset 2, 3, and 4). However, their performance deteriorates with respect to that of blob detectors on high spatial-resolution images (e.g., Datasets 1 and 5). For instance, BRISK-based RRN on Dataset 1 and 5 results in normalized subjects image, which are not as vivid as the blob detectors' results. Moreover, the normalized images generated using ORB-based RRN show color distortions on the high spatial-resolution datasets. The performance loss of corner detectors can be attributed to why the RCS extracted by these methods are object corners often considered point-wise properties [30] and thereby are typically affected by sharp intensity changes and occlusion boundaries. Therefore, they are more sensitive to temporal changes than the blob detectors, resulting in generating the deteriorated normalized subject images, especially for high-resolution datasets. It can also be seen from rose graphs in Fig. 4(c) that the correlation values between DN of inliers generated by corner detectors are much less than that of blob detectors, which justifies why their results are relatively inferior. For Datasets 2, 3, and 4, about 25% of inliers generated by the corner detectors had nearly high correlation values (≥ 0.75). The results in Fig. 4(b) show that a high number of matched keypoints (or the size of the RCS) between the reference and subject images does not necessarily mean that the corresponding normalized image would have higher quality. For instance, SIFT consistently detects the highest number of matches; however, its performance is not best for all datasets.

It is necessary to have a sufficient number of keypoint matches in the RCS with a representative spatial distribution to estimate the correct normalization coefficients. Moreover, the keypoint detectors/descriptors considered in this article cannot seamlessly detect features over textured and textureless areas, which deteriorates the performance on datasets with large areas without patterns (e.g., water bodies). It is mainly because these methods inherently select the local image features from surfaces having good patterns to secure keypoint detection and description [31]. With this in mind, the blob detectors SURF, SIFT, KAZE, and AKAZE performed better than the corner detectors ORB and BRISK in RRN for most cases. This is because blobs include

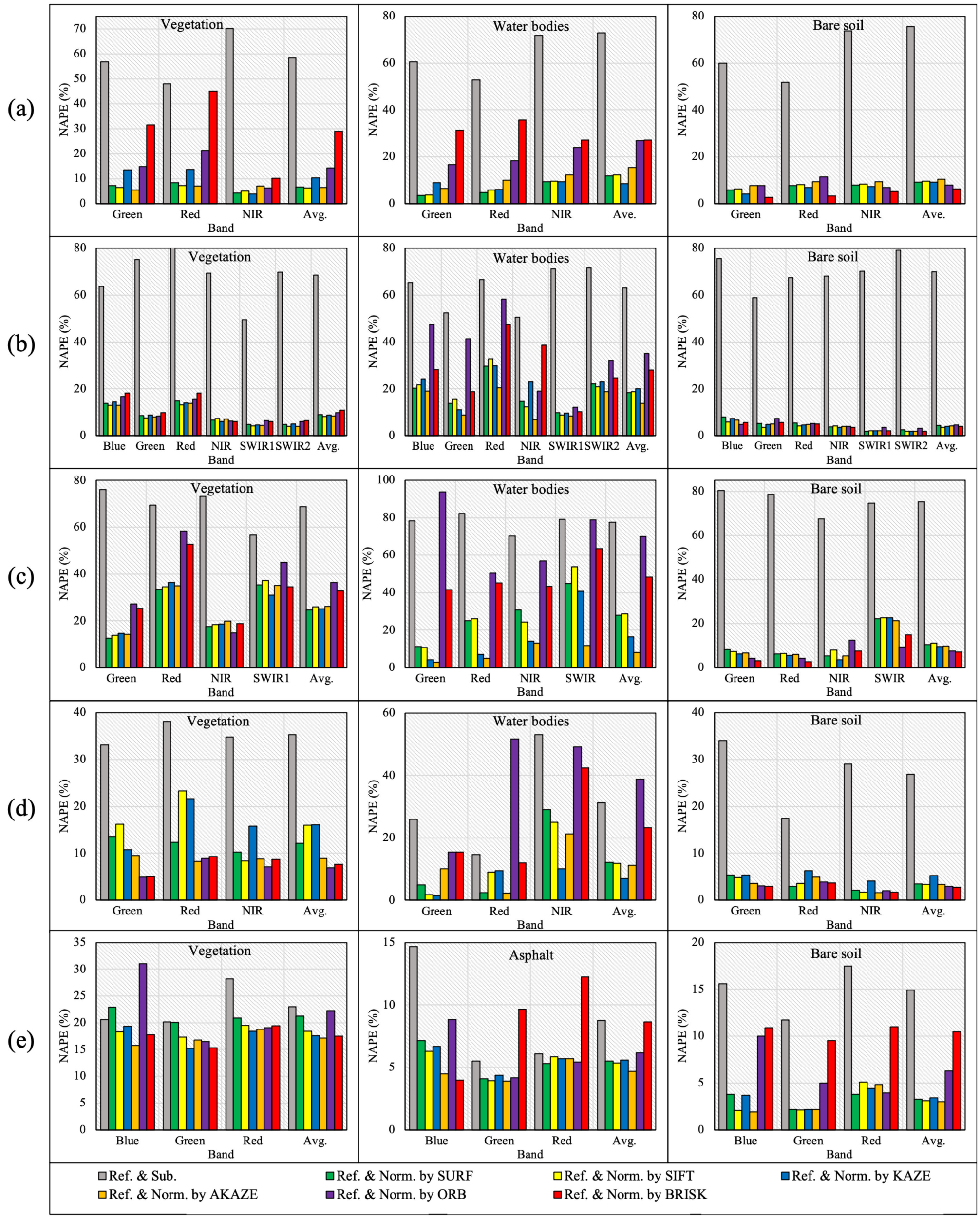

Fig. 5. Comparison of the MAPE values between the reference and subject images and the reference and normalized subject images generated by keypoint-based RRN with different keypoint detectors/descriptors over of vegetation, bare soils, water bodies, and asphalt (only for Dataset 5) for Datasets 1(a)-5(e).

more detailed information on local feature regions and reflect better their characteristics under various radiometric and geometric distortions (e.g., differences in illumination, rotation, and scale) between image pairs [32].

The MAPE values before and after RRN are compared over test samples of different LULC classes to evaluate the local performance of keypoint-based RRN [see Fig. 5(a)–(e)]. To this end, multiple polygons from different LULC classes on the overlapped areas of reference, subject, and normalized images were considered.

It can be seen from Fig. 5 that the MAPE values of LULC classes are generally reduced after normalizing subject images of Datasets 1-5, using keypoint-based RRN with different detectors/descriptors. The corner detectors resulted in the highest MAPE values for vegetation, water bodies, and asphalt classes, indicating a low capability of these methods in correcting radiometric distortions from these classes compared to that of the blob detectors. For instance, the MAPE values between the normalized subject images generated by corner detectors (ORB and BRISK) and the reference images were close to those between the subject and reference images and sometimes even higher, especially for Dataset 5 in Fig. 5(e). However, the BRISK performed better than the other keypoint detectors/descriptors in reducing radiometric distortions from bare soils for Datasets 1, 3, and 4, while SURF and KAZE performed better, respectively, for Dataset 2 and Dataset 5. SIFT, SURF, ORB, and AKAZE achieved the most significant effect in normalizing vegetation's radiometric properties for Dataset 1, Dataset 2, Dataset 3,

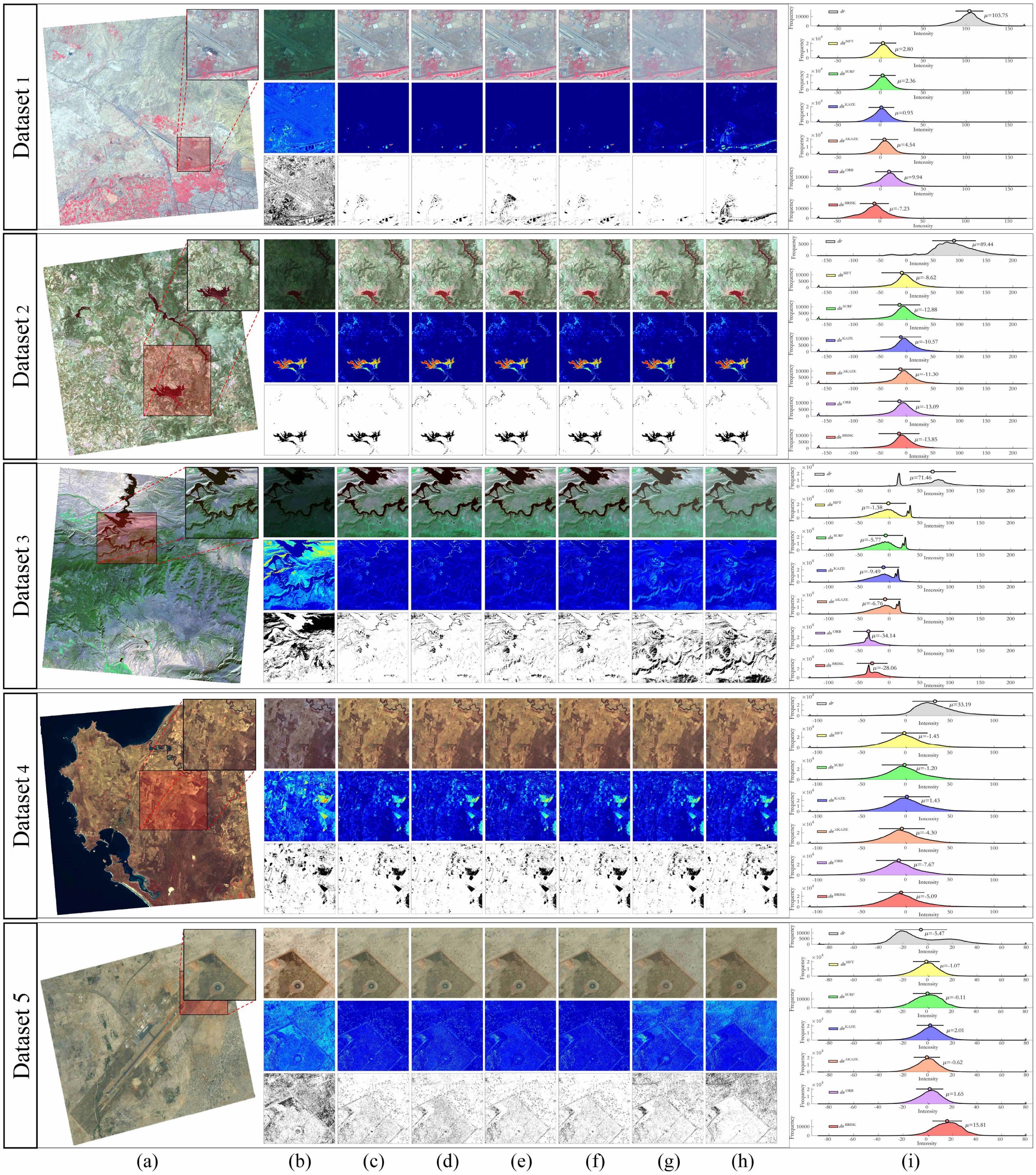

Fig. 6. Change detection and RRN results before and after applying keypoint-based RRN methods on Datasets 1-5. (Top row) Normalized subject images, (middle row) difference images, and (Bottom row) change maps generated based on applying keypoint-based RRN with (c) SIFT, (d) SURF, (e) KAZE, (f) AKAZE,(g) ORB, and (h) BRISK, on reference and subject images in (a) and (b); and (i) Comparison of the difference histogram of the reference and subject images (d_r), and the difference histogram of the reference and normalized images (d_n) in the Red band of Datasets 1 to 5.

Dataset 4, and Dataset 5, respectively. AKAZE was the most effective keypoint detector/descriptor in rectifying radiometric distortions of asphalt for Dataset 5. KAZE and AKAZE were the most efficient keypoint detectors/descriptors in correcting radiometric preterites of water bodies for Datasets 1 and 4 and Dataset 2 and 3, respectively.

The difference images and change maps are specifically employed to support visual comparisons between reference and normalized subject images. Before processing, the subject and normalized subject images are carefully registered to corresponding reference images using inliers. The difference images are then generated using change vector analysis (CVA) [33] technique. Finally, Otsu's thresholding method [34] is applied to them for producing change maps, in which "1" (or white) means unchanged and "0" (or black) denotes changed. The normalized subject images, difference images, and change maps for part of each of the datasets resulting from keypoint-based RRN methods are demonstrated in Fig. 6(a)–(e). Moreover,

TABLE V
SUMMARY OF THE PERFORMANCE OF KEYPOINT-BASED RRN FOR DIFFERENT KEYPOINT DETECTORS/DESCRIPTORS IN TERMS OF ACCURACY FOR THE ENTIRE IMAGE (OVERALL) AND LULC CLASSES, QUANTITY AND QUALITY OF KEYPOINTS IN THE RCS, VISUAL QUALITY, AND SPEED (COMPUTING TIME)

Algorithm	Accuracy		RCS		Visual Quality	Speed
	Overall	LULC	Quality	Quantity		
SURF	●●	●●●	●●●	●●●	●●●●	●●
SIFT	●●●●	●●●	●●●●	●●●●	●●●●	●
KAZE	●●●	●●●	●●●	●●●	●●●●	●●
AKAZE	●●	●●●●	●●●	●●●	●●●●	●●●
ORB	●	●	●●	●●	●●	●●●●
BRISK	●●	●●	●●	●●●	●●	●●●

One bullet denotes the worst performance, while four bullets refers to the best performance.

the difference histograms of the reference and subject images (d_r) to those of the reference and normalized images (d_n) (i.e., generated by keypoint-based RRN methods) in the red band for all datasets are demonstrated in Fig. 6 (i).

As shown in Fig. 6(a)–(e), one can visually observe that the change detection results generated from the reference and normalized subject images are more accurate compared to those of the reference and original subject images for all datasets. For example, the noise and anomalies have significantly prevailed in the difference images generated from the reference and original subject images in most cases except for Dataset 2, where the valid changes were not well highlighted. This is mainly due to the existing radiometric differences (e.g., temporal variations in atmospheric conditions, soil color, and illumination changes) between the reference and original subject images, resulting in potential false/miss detections in the change maps. The normalized subject images in (b)-(e) indicate that SIFT-, SURF-, KAZE-, AKAZE-based RRN yield visually similar results better than those produced by ORB- and BRISK-based RRN. Likewise, the difference images and change maps under the RRN using blob detectors are less affected by the outliers and more in line with the real changed regions (i.e., happened between the image pairs) than those under the RRN using corner detectors, especially for Datasets 1, 3, and 5. For example, the RRN using ORB and BRISK detectors was not able to handle phenological variations (i.e., induced by the growth of plants) adequately for Dataset 4, thus resulting in noisy change detection products. This is mainly because a significant amount of complementary information content about points and/or regions is not considered by corner detectors in the RRN procedure.

As observed in Fig. 6(i) histograms of d_n have approximately bell-shaped distribution and are narrower than the curves of (d_r) for all datasets. This is because the histograms of d_r have been shifted to zero and near-zero position (the unchanged part) after radiometric calibration by the keypoint-based RRN methods. Among these methods, the mean of the blob histograms' curves are closer to zero value than curves of $d_r^B RISK$ and $d_r^O RB$ for all datasets, indicating the capability of blob detectors in RRN of image pairs. For example, KAZE-, SIFT-, and SURF-based RRN have a minimum mean of the curves, respectively, for the red band of Dataset 1, Datasets 2 and 3, Datasets 4 and 5.

The overall summary of the above analysis is given in Table V. It is clear that SIFT-based RRN achieves the best performance in all categories except the computing time, which is the worst among all keypoint detectors/descriptors. SURF-based RRN performs its operations faster with respect to the SIFT-based RRN at the expense of losing accuracy and the RCS. KAZE- and AKAZE-based RRN achieves a good balance between all categories, making them suitable for RRN of unregistered bitemporal remote sensing images. Although ORB-based RRN is the fastest, its performance in other categories is inferior to the other keypoint-based RNN methods.

IV. CONCLUSION

This article proposed a keypoint-based method for RRN of unregistered bitemporal multispectral images. It evaluated the performances of different keypoint detectors/descriptors on datasets showing variations in terms of spatial-resolution and instruments. The experimental results show that keypoint-based RRN can satisfactorily normalize bitemporal image pairs showing high variations in terms of spatial-resolution, illumination, and sensors. The blob detectors (SURF, SIFT, KAZE, and AKAZE) are more accurate on average than the corner detectors (ORB and BRISK) in RRN; however, they are slower in computing. Thus, there is a balance between accuracy and computing time. KAZE and AKAZE-based RRN can achieve a good tradeoff between these two metrics. Although the use of the keypoint-based RRN method has shown promising results, large texture-less areas in the images can negatively affect its results.

This study has shown the potential of keypoint-based RRN for the most commonly used keypoint detectors/descriptors from the literature. As a future work, one can explore advanced keypoint detectors/descriptors to achieve better results.

REFERENCES

[1] A. Moghimi, A. Mohammadzadeh, T. Celik, and M. Amani, "A novel radiometric control set sample selection strategy for relative radiometric normalization of multitemporal satellite images," *IEEE Trans. Geosci. Remote Sens.*, vol. 59, no. 3, pp. 2503–2519, Mar. 2021.

[2] W. Bonnet and T. Celik, "Random sampling-based relative radiometric normalization," *IEEE Geosci. Remote Sens. Lett.*, to be published, doi: 10.1109/LGRS.2020.3047344.

[3] M. Omati and M. R. Sahebi, "Change detection of polarimetric SAR images based on the integration of improved watershed and MRF segmentation approaches," *IEEE J. Sel. Top. Appl. Earth Observ. Remote Sens.*, vol. 11, no. 11, pp. 4170–4179, Nov. 2018.

[4] M. Amani *et al.*, "Application of Google Earth engine cloud computing platform, Sentinel imagery, and neural networks for crop mapping in Canada," *Remote Sens.*, vol. 12, no. 21, 2020, Art. no. 3561.

[5] T. Celik and H. Demirel, "Fire detection in video sequences using a generic color model," *Fire Saf. J.*, vol. 44, no. 2, pp. 147–158, 2009.

[6] T. Celik, "Unsupervised change detection in satellite images using principal component analysis and k-means clustering," *IEEE Geosci. Remote Sens. Lett.*, vol. 6, no. 4, pp. 772–776, Oct. 2009.

[7] F. D. Javan, F. Samadzadegan, S. Mehravar, A. Toosi, R. Khatami, and A. Stein, "A review of image fusion techniques for pan-sharpening of high-resolution satellite imagery," *ISPRS J. Photogrammetry Remote Sens.*, vol. 171, pp. 101–117, 2021.

[8] X. Li, R. Feng, X. Guan, H. Shen, and L. Zhang, "Remote sensing image mosaicking: Achievements and challenges," *IEEE Geosci. Remote Sens. Mag.*, vol. 7, no. 4, pp. 8–22, Dec. 2019.

[9] A. Moghimi, A. Sarmadian, A. Mohammadzadeh, T. Celik, M. Amani, and H. Kusetogullari, "Distortion robust relative radiometric normalization of multitemporal and multisensor remote sensing images using image features," *IEEE Trans. Geosci. Remote Sens.*, to be published, doi: 10.1109/TGRS.2021.3063151.

[10] M. J. Canty and A. A. Nielsen, "Automatic radiometric normalization of multitemporal satellite imagery with the iteratively re-weighted mad transformation," *Remote Sens. Environ.*, vol. 112, no. 3, pp. 1025–1036, 2008.

[11] P. R. Marpu, P. Gamba, and M. J. Canty, "Improving change detection results of IR-MAD by eliminating strong changes," *IEEE Geosci. Remote Sens. Lett.*, vol. 8, no. 4, pp. 799–803, Jul. 2011.

[12] Y. Bai, P. Tang, and C. Hu, "KCCA transformation-based radiometric normalization of multi-temporal satellite images," *Remote Sens.*, vol. 10, no. 3, pp. 1–21, 2018, 432, doi: 10.3390/rs10030432.

[13] L. G. Denaro and C.-H. Lin, "Hybrid canonical correlation analysis and regression for radiometric normalization of cross-sensor satellite imagery," *IEEE J. Sel. Top. Appl. Earth Observ. Remote Sens.*, vol. 13, pp. 976–986, 2020.

[14] H. Zhou, S. Liu, J. He, Q. Wen, L. Song, and Y. Ma, "A new model for the automatic relative radiometric normalization of multiple images with pseudo-invariant features," *Int. J. Remote Sens.*, vol. 37, no. 19, pp. 4554–4573, 2016.

[15] S. A. K. Tareen and Z. Saleem, "A comparative analysis of Sift, Surf, Kaze, Akaze, Orb, and Brisk," in *Proc. Int. Conf. Comput., Math. Eng. Technol.*, 2018, pp. 1–10.

[16] D. G. Lowe, "Distinctive image features from scale-invariant keypoints," *Int. J. Comput. Vis.*, vol. 60, no. 2, pp. 91–110, 2004.

[17] H. Bay, T. Tuytelaars, and L. Van Gool, "Surf: Speeded up robust features," in *Proc. Eur. Conf. Comput. Vis.*, 2006, pp. 404–417.

[18] P. F. Alcantarilla, A. Bartoli, and A. J. Davison, "Kaze features," in *Proc. Eur. Conf. Comput. Vis.*, 2012, pp. 214–227.

[19] M. Agrawal, K. Konolige, and M. R. Blas, "Censure: Center surround extremas for realtime feature detection and matching," in *Proc. Eur. Conf. Comput. Vis.*, 2008, pp. 102–115.

[20] P. F. Alcantarilla and T. Solutions, "Fast explicit diffusion for accelerated features in nonlinear scale spaces," *IEEE Trans. Pattern. Anal. Mach. Intell*, vol. 34, no. 7, pp. 1281–1298, Oct. 2011.

[21] E. Rublee, V. Rabaud, K. Konolige, and G. Bradski, "ORB: An efficient alternative to sift or surf," in *Proc. IEEE Int. Conf. Comput. Vis.*, 2011, pp. 2564–2571.

[22] E. Rosten and T. Drummond, "Machine learning for high-speed corner detection," in *Proc. Eur. Conf. Comput. Vis.*, 2006, pp. 430–443.

[23] M. Calonder, V. Lepetit, C. Strecha, and P. Fua, "Brief: Binary robust independent elementary features," in *Proc. Eur. Conf. Comput. Vis.*, 2010, pp. 778–792.

[24] S. Leutenegger, M. Chli, and R. Y. Siegwart, "Brisk: Binary robust invariant scalable keypoints," in *Proc. IEEE Int. Conf. Comput. Vis.*, 2011, pp. 2548–2555.

[25] V. Balntas, K. Lenc, A. Vedaldi, and K. Mikolajczyk, "Hpatches: A benchmark and evaluation of handcrafted and learned local descriptors," in *Proc. IEEE Conf. Comput. Vis. Pattern Recognit.*, 2017, pp. 5173–5182.

[26] M. A. Fischler and R. C. Bolles, "Random sample consensus: A paradigm for model fitting with applications to image analysis and automated cartography," *ACM Commun.*, vol. 24, no. 6, pp. 381–395, 1981.

[27] Q. Chen, S. Wang, B. Wang, and M. Sun, "Automatic registration method for fusion of ZY-1-02C satellite images," *Remote Sens.*, vol. 6, no. 1, pp. 157–179, 2014.

[28] S.-J. Chen, H.-L. Shen, C. Li, and J. H. Xin, "Normalized total gradient: A new measure for multispectral image registration," *IEEE Trans. Image Process.*, vol. 27, no. 3, pp. 1297–1310, Mar. 2017.

[29] A. Vedaldi and B. Fulkerson, "VLFeat: An open and portable library of computer vision algorithms," 2008. [Online]. Available: http://www.vlfeat.org/

[30] T. Lindeberg, *Scale-Space Theory in Computer Vision*, vol. 256. New York, NY, USA: Kluwer Academic Publishers, 1994.

[31] F. Tombari, A. Franchi, and L. Di Stefano, "Bold features to detect textureless objects," in *Proc. IEEE Int. Conf. Comput. Vis.*, 2013, pp. 1265–1272.

[32] X. Xiong and B.-J. Choi, "Comparative analysis of detection algorithms for corner and blob features in image processing," *Int. J. Fuzzy Log. Intell. Syst.*, vol. 13, no. 4, pp. 284–290, 2013.

[33] W. A. Malila, "Change vector analysis: An approach for detecting forest changes with landsat," in *Proc. LARS Symposia*, 1980, pp. 326–335.

[34] N. Otsu, "A threshold selection method from gray-level histograms," *IEEE Trans. Syst., Man, Cybern.*, vol. 9, no. 1, pp. 62–66, Jan. 1979.

Armin Moghimi received the B.Sc. degree in geomatics engineering from the Geomatics College, Iran National Cartographic Center, Tehran, Iran, in 2013, and the M.Sc. degree in photogrammetry engineering in 2015 from the K. N. Toosi University of Technology, Tehran, Iran, where he is currently working toward the Ph.D. degree in photogrammetry and remote sensing.

His research interests include change detection techniques, image preprocessing, image registration, machine learning, SAR image processing, and LiDAR data processing.

Turgay Celik (Member, IEEE) received the second Ph.D. degree from the University of Warwick, Coventry, U.K., in 2011.

He is currently a Professor in digital transformation and the Director at the Wits Institute of Data Science with the University of Witwatersrand, Johannesburg, South Africa. His research interests include signal and image processing, computer vision, machine intelligence, robotics, data science and remote sensing.

Dr. Celik is an Associate Editor for the *IET ELL*, IEEE GEOSCIENCE AND REMOTE SENSING LETTERS, IEEE JOURNAL OF SELECTED TOPICS IN APPLIED EARTH OBSERVATIONS AND REMOTE SENSING, and Springer's *SIVP*.

Ali Mohammadzadeh received the Ph.D. degree in remote sensing from Geomatics Engineering faculty of K.N. Toosi University of Technology, Tehran, Iran, in 2009.

He is currently an Associate Professor and Head of LiDAR Laboratory at K.N. Toosi University of Technology. He has more than 40 published journal papers and his research interests are LiDAR, artificial intelligence, image processing and pattern recognition, physics of remote sensing, optimization, sensor calibration, disaster management in dust, earthquake, and flooding.

Huseyin Kusetogullari (Member, IEEE) received the Ph.D. degree from the University of Warwick, Coventry, U.K., in 2012.

He is currently working as a Senior Lecturer with the Department of Computer Science, Blekinge Institute of Technology and School of Informatics, University of Skövde. His research interests are in the areas of image and video processing, artificial intelligence, evolutionary methods and remote sensing.